PHYSICAL REVIEW B **77**, 214110 (2008)

Structure of epitaxially grown rare-earth intermetallics using x-ray diffraction: RT_2, RT_3, RT_5, and R_2T_{17}

S. R. Jones,* A. Dunhill, R. A. Cowley, and R. C. C. Ward
Department of Physics, University of Oxford, Oxford, OX1 3PU, United Kingdom

(Received 6 February 2008; revised manuscript received 25 April 2008; published 18 June 2008)

X-ray diffraction measurements have been made on a series of molecular beam epitaxy (MBE)-grown RT_2, RT_3, RT_5, and R_2T_{17} thin layer samples, where R=Er, Nd, and T=Co, Fe, and RT_2 superlattice samples, where R=Er, Nd, Y, and T=Fe. These measurements show that it is possible to grow RT_2 materials by MBE techniques, using a Mo[110] buffer, with the [111] cubic direction as the growth axis and to grow RT_3 and R_2T_{17} materials, using the same Mo[110] buffer, with the [001] rhombohedral or hexagonal axis as the growth axis. In addition, $RT_{2.2}$ materials and R_2T_{17} with an excess of R were grown and it was found that the materials separated into two commensurate epitaxial phases: RT_2+RT_3 and R_2T_{17}+RT_3. We found that it was not possible to grow RT_5 by these MBE techniques. The magnetization of the thin layers of $ErCo_3$, $NdCo_3$, Er_2Co_{17}, and Nd_2Co_{17} was also measured using a superconducting quantum interference device (SQUID) magnetometer. Measurements show that the magnetization of $NdCo_3$ and Er_2Co_{17} is larger in the layers compared to bulk properties, the magnetization of the Nd_2Co_{17} layer is similar to that of the bulk material and the magnetization and also the Curie temperature, 195 K, of the $ErCo_3$ layer are lower than those of the bulk material which has a Curie temperature of 395 K.

DOI: 10.1103/PhysRevB.77.214110 PACS number(s): 61.05.cp, 75.70.Ak

I. INTRODUCTION

There is a long history of research into the rare earth–transition metal (R-T) intermetallic compounds in bulk form based on the idea that the R and T atoms will interact to give useful properties. Their magnetic moments couple ferromagnetically where R is a light rare earth and antiferromagnetically where R is a heavy rare earth and magnetic interactions are possible that will raise the ordering temperature of the elemental rare earths—which have large localized moments—to above room temperature. This is the basis for the permanent magnet compounds RT_5 and R_2T_{17} which are widely used in electric motors and other magnetomechanical devices.

Magnetic multilayer films of these compounds have become a subject of research due to their possible applications as permanent magnets.[1] It has been shown that it should be possible to substantially increase the energy product in oriented nanostructured two-phase magnets by exploiting the exchange coupling between hard and soft layers.[2] Such magnets have potential applications in sensors and recording media.[3] In these structures the hard regions act as a skeleton to stiffen the magnetization direction of the soft regions, increasing the coercivity of the sample while the soft layers contribute an increase in the magnetic remanence, M_r.

Recently it has become possible to grow the Laves phase RT_2 materials as epitaxial thin films or as superlattices. These have large magnetic moments which are very dependent on the exact composition and strain of the material.[1] The properties of the material can therefore be tailored to produce devices for specific applications as magnetostrictive materials or the sensors and memory devices mentioned above. This work is a natural extension of research into the bulk material in the 1970s[4] and of the work on superlattices of the rare-earth metals in the 1990s.[5,6]

So far experiments have concentrated on the cubic Laves RT_2 materials grown on a substrate of sapphire upon which a niobium buffer layer is deposited, followed by a 20 Å-thick iron seed layer. The RT_2 superlattice is then grown on top. With this system the Laves phase can be grown with the cubic [110] direction perpendicular to the growth planes. It has then been shown to be possible to grow single films of RT_2 with R any rare earth and T Fe or Co. Superlattices of the materials have only been grown of those materials with Fe as the transition metal because if other transition metals are used, interdiffusion prohibits the growth of the superlattice.

The successful growth of $DyFe_2/YFe_2$ superlattices, which have magnetic moments aligned largely perpendicular to the growth direction, has demonstrated unusual exchange spring behavior as well as the existence of spin-flop phases in Y-rich materials.[7,8] The direction of the moments, however, depends on the composition of the superlattice. $ErFe_2/YFe_2$ superlattices have also been grown and have the magnetic moments aligned largely along the growth direction. Magnetization measurements show that in an applied field they also show exchange spring behavior.[9]

It is difficult to grow compounds with different compositions such as RT_3, RT_5, and R_2T_{17} using the same method as that described above for RT_2 compounds, but some growth of nonLaves phase compounds has been achieved by various methods. Fully epitaxial Y_2Co_{17} has been grown on W(100),[10] SmCo $(1\bar{1}00)$ and $(11\bar{2}0)$ films have been grown by magnetron sputtering onto Chromium buffered MgO (Ref. 11) and $Nd_2Fe_{14}B(001)$ has been grown on Mo(001).[12]

We anticipate that Mo(110) might act as a universal substrate for epitaxy of the Laves phase RT_2 compounds along the cubic [111] axis and other R-T compounds, either rhombohedral or hexagonal, along the hexagonal [0001] axis. This orientation has the advantage of having the easy axis of magnetization along the growth axis which is of use for applications in, for example, data storage media.

The solution that we use was found by Robaut *et al.*[13] and Huth and Flynn[14] who used either molybdenum or tungsten as a buffer. Both of these materials grow on sapphire with the [110] direction parallel to the growth direction and then the RT_2 materials have a [111] axis along the growth direction. This change of axis not only alters the properties of the superlattice but also enables the growth of single crystal films and superlattices of RT_3 and R_2T_{17}.

In this paper we report on the growth and characterization of a range of these materials. The structure and orientation of the superlattices and single films were determined by x-ray scattering techniques using a PANalytical Materials Research Diffractometer (MRD). We have also measured the magnetization of a few of the materials and have shown that the thin films of some of the compounds are very strong hard magnets.

Section II of the paper describes in detail how the structures are grown and the precise orientation of the different planes through the epitaxial structures. Section III describes the crystal structure of the bulk materials RT_2, RT_3, RT_5, and R_2T_{17} and the way in which they can be distinguished by careful use of x-ray scattering techniques. Section IV describes the results that were obtained from both the x-ray measurements and the magnetization measurements. The results are summarized and discussed in Sec. V.

The growth of some of the samples described in this paper, in particular the RT_5 composition, was unsuccessful. We have described most of the results because this experience may guide those following even where we were not wholly successful. We hope that this paper will lead to considerably more work which will exploit the magnetic properties of these materials to make useful devices.

II. EXPERIMENTAL ARRANGEMENTS

A. Sample growth

The samples investigated in this paper are as shown in Table I. The notation used for the superlattices is $[t_1\ \text{Å}\ \text{ErFe}_2/t_2\ \text{Å}\ \text{YFe}_2]_N$, where t_1 and t_2 are the nominal thicknesses in Angstroms of the $ErFe_2$ layers and N is the number of layers.

The samples were prepared in the Balzers facility, Oxford using molecular beam epitaxy (MBE). They are grown as follows. For both thin films and superlattices a sapphire substrate with a $[11\bar{2}0]$ orientation is used and then a single 250 Å (for thin films) or 500 Å (for superlattices) layer of (110) molybdenum was deposited at 1120 K as a buffer. The R-T film is grown by co-deposition of the elemental fluxes in the correct stoichiometric ratios. This was done at 970 K cooling during growth to 720 K. Lastly a cap of either 100 Å of molybdenum or 100 Å of yttrium (for the $[50\text{ErFe}_2/100\text{YFe}_2]_{40}$, $[75\text{ErFe}_2/75\text{YFe}_2]_{40}$ and Y_2Co_{17} samples) was deposited.

B. X-ray diffraction measurements

The structure of the films was determined using a PANalytical MRD. The diffractometer was used with a four bounce Ge monochromator and a focusing mirror to focus the Cu k_α x rays. The scattered x rays were measured mostly with a slit before the detector with a width of $\frac{1}{4}°$. Some measurements were made with a three bounce Ge analyzer and others with a slit of width 1°. All of the measurements were made at room temperature with the samples in air.

TABLE I. Observed crystal structures of the samples studied. M is the mosaic spread, (*r.*) indicates a rhombohedral structure and (h.) indicates a hexagonal structure. The structures of the compounds observed in the samples $ErCo_{2.2}$ and $YCo_{\simeq 2.2}$ are given in Sec. IV D.

Sample	Structure	*a* (Å)	*c* (Å)
4000 Å $ErFe_2$	$MgCu_2$ (*r.*) [a]	4.947(93)	12.5498(2)
2000 Å $ErCo_2$	$MgCu_2$ (*r.*) [a]	5.064(9)	12.3555(5)
$[50\text{ErFe}_2/100\text{YFe}_2]_{40}$	$MgCu_2$ (*r.*) [a]	5.152(9)	12.6359(4)
$[75\text{ErFe}_2/75\text{YFe}_2]_{40}$	$MgCu_2$ (*r.*) [a]	5.175(9)	12.6294(9)
2650 Å $ErCo_3$	$PuNi_3$ (*r.*)	5.035(9)	24.1807(1)
2650 Å $NdCo_3$	$PuNi_3$ (*r.*)	5.067(9)	24.6451(1)
1750 Å $ErCo_5$	$CaCu_5$ (*h.*)		4.0528(4)
2200 Å $NdCo_5$	$CaCu_5$ (*h.*)		4.079(5)
1000 Å $ErCo_{2.2}$			
4000 Å $YCo_{\simeq 2.2}$			
1550 Å Er_2Co_{17}	Th_2Ni_{17} (*h.*) [b]	8.322(24)	8.1526(16)
1250 Å Nd_2Co_{17}	Th_2Zn_{17} (*r.*) [b]	8.437(17)	12.2398(2)
2600 Å Y_2Co_{17}	Th_2Ni_{17} (*h.*) [b]		8.2945(10)

[a] These compounds are rhombohedral due to a slight distortion of the bulk cubic structure (see Sec. III A for details).

[b] Our measurements could not distinguish between the rhombohedral and hexagonal structures for the R_2T_{17} compounds.

The samples were oriented with the growth axis horizontal and in the scattering plane. The reciprocal space is shown schematically in Fig. 1 and the shaded areas show the regions that cannot be observed either because the incident or scattered beam must penetrate the substrate or because the scattering angle becomes too large. A scan of the wave-vector transfer perpendicular to the plane of the sample and along the growth direction is known as a longitudinal on-axis scan and determines the nature of the planes perpendicular to the growth direction. Scans for which the wave-vector transfer is perpendicular to q_z and through the Bragg reflections are called transverse scans and enable the mosaic spread to

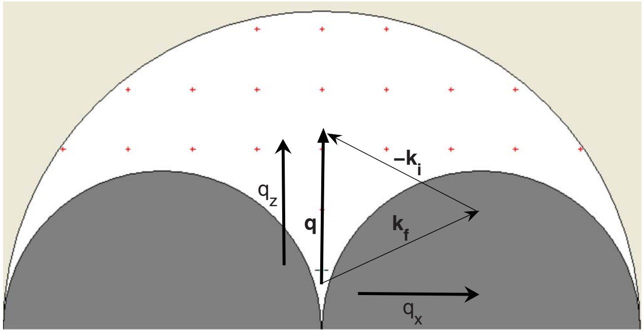

FIG. 1. (Color online) Schematic of the scattering plane. The shaded areas are the regions of reciprocal space that cannot be observed because either the incident or scattered beam must penetrate the sample, or because the scattering angle becomes too large.

TABLE II. Crystal structures of bulk RT_2, RT_3, RT_5 and R_2T_{17} compounds. Data taken from Ref. 4.

Compound	Crystal structure	a (Å)	c (Å)	T_c
$ErCo_2$	$MgCu_2$ (rhombohedral)	5.055	12.36	38.8
$ErFe_2$	$MgCu_2$ (rhombohedral)	5.150	12.61	587
$ErCo_3$	$PuNi_3$ (rhombohedral)	4.972	24.18	395
$NdCo_3$	$PuNi_3$ (rhombohedral)	5.060	24.78	392.6
$ErCo_5$	$CaCu_5$ (hexagonal)	4.870	4.002	10(1)
$NdCo_5$	$CaCu_5$ (hexagonal)	5.020	3.977	910
YCo_5	$CaCu_5$ (hexagonal)	4.935	3.964	987
Er_2Co_{17}	Th_2Ni_{17} (hexagonal)	8.310	8.113	1184
Nd_2Co_{17}	Th_2Zn_{17} (rhombohedral)	8.407	12.257	1157
Y_2Co_{17}	Th_2Ni_{17} (hexagonal)	8.341	8.125	1186

be obtained. Scans of the wave-vector transfer parallel to the longitudinal on-axis scans but through different Bragg reflections are known as off-axis scans and enable the orientation and structure of the planes to be determined.

The MRD enables different scattering planes to be measured by using the ϕ angle whose rotation axis is aligned along the growth direction $(0\ 0\ 0\ q_z)$ (as most of the compounds studied are rhombohedral and described using a hexagonal unit cell, the hexagonal four-index notation will be used). Scans of the intensity when ϕ is varied enable further information to be obtained about the orientation of the growth planes.

Due to the angular restrictions on the measurements, the on-axis scans were performed with wave-vector transfers between zero and 6.5 Å including both the reflectivity and diffraction peaks. The off-axis peaks were measured from values of $q_z=3.1$ Å to 6.5 Å along the $(1\ 0\ \bar{1}\ l)$ series of reflections and from $q_z=3.75$ Å to 6.7 Å along the $(1\ 1\ \bar{2}\ l)$ series. In the interests of clarity, only a part of these scans is illustrated in the figures showing the results.

C. Magnetometer measurements

The magnetization measurements were carried out using the dc method on a superconducting quantum interference device (SQUID). The SQUID magnetometer used was a Quantum Design model MPMSXL. The instrument has a sample environment capable of reaching a base temperature of just below 2 K. Operation and data acquisition are controlled by computer. Measurements were taken at fields between −5 T and 5 T and at temperatures between 50 K and 200 K. The volume of the sapphire substrate is very much larger than that of the Laves phase films (the substrate has a thickness of 1 mm while the thin films have only a couple of thousand Angstroms) so the diamagnetic magnetization of the sapphire is large in comparison to the magnetization of the Laves phases. The substrate diamagnetism (with a value of the susceptibility of $\chi=-4.4(1)\times10^{-1}$ emu Oe^{-1} g^{-1} from measurements of just the sapphire substrate) was therefore subtracted from the data to enable the magnetization of the Laves phases to be seen clearly.

III. THEORY

A. Scattering from the layers

The structures of bulk RT_2, RT_3, RT_5, and R_2T_{17} compounds are known to be as shown in Table II.[4] Initially these different structures appear to be very complex and to change drastically from one composition to the next. However, as pointed out by Buschow,[4] the structures are all related to one another. The simplest compound is RT_5 which has the hexagonal $CaCu_5$ structure and consists of alternating planes with compositions of RT_2 and T_3 stacked along the hexagonal [0001] axis with identical planes having a separation along this axis that is slightly less than 4 Å. This structure is shown schematically in Fig. 2. Despite the relative simplicity of the structure it is expected that there will be some difficulty in growing the RT_5 compounds. The difficulty can be explained with reference to the phase diagram in Fig. 3 which shows the Gd-Co phase diagram—typical of the R-T intermetallic compounds. It can be seen that there is no stable $GdCo_5$ phase below 775 °C, instead two adjacent phases, Gd_2Co_7 and Gd_2Co_{17} are expected to form. Bulk RT_5 materials are prepared by quenching from high temperature; MBE growth between 700 °C and 400 °C was attempted in the hope of overcoming the thermodynamics of the system

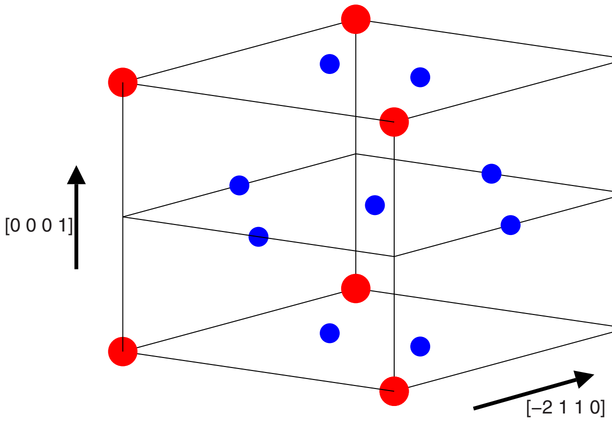

FIG. 2. (Color online) Unit cell of RT_5 structure. The rare-earth atoms are represented by large (red online) circles and transition metal atoms by smaller (blue online) circles.

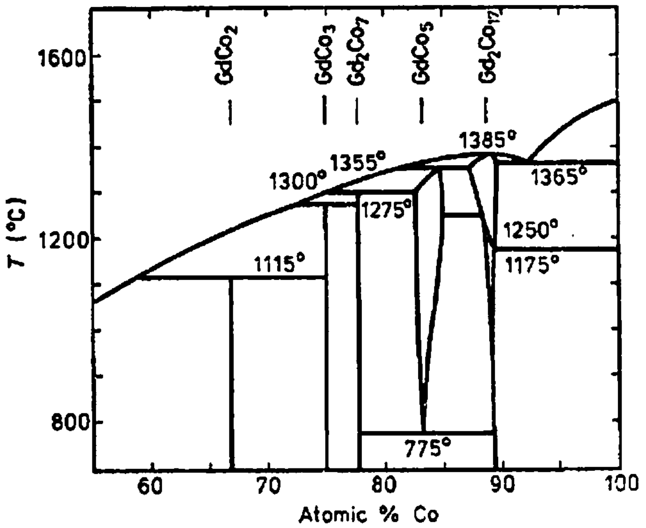

FIG. 3. Phase diagram of Gd-Co system. After Buschow (Ref. 4).

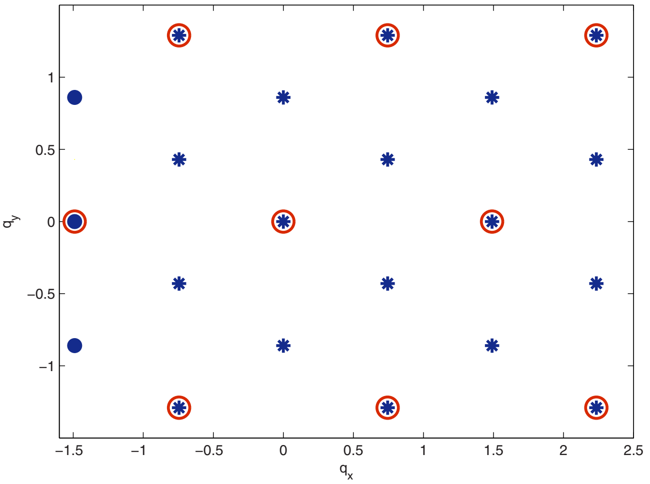

FIG. 4. (Color online) Reciprocal lattices of R_2T_{17} (stars) and RT_3 (circles). The plane shown is the *xy* plane, perpendicular to the hexagonal [001] growth direction.

and stabilizing the high-temperature structure by epitaxy.

The RT_3 ($PuNi_3$ rhombohedral) structure is obtained by replacing T atoms with R atoms in the RT_5 structure. This occurs in alternate RT_2 planes so that the structure has successive planes $RT_2-T_3-R_2T-T_3-RT_2$. This is accompanied by a layer shift so that the structure only repeats after three sets of these four planes. The *c*-axis lattice parameter thus becomes approximately six times longer than in the RT_5 cell. This rhombohedral structure will be described using a hexagonal unit cell and the growth direction is hence along the hexagonal [0001] axis.

The RT_2 structure is made up from one set of planes containing only R atoms and one slightly buckled plane containing two T atoms. This set of two planes is repeated three times so that the unit cell along the hexagonal axis is then somewhat more than three times as long as that for the RT_5 material. In bulk this material is cubic, with the cubic $MgCu_2$ structure, however, in the epitaxial layers this cubic symmetry is broken. There is a contraction or expansion along the growth direction, in this case the cubic $[111]_C$ direction, and the structure of the RT_2 films becomes rhombohedral. This rhombohedral structure will be described using a hexagonal unit cell with the hexagonal [0001] axis along the growth direction.

Finally we discuss the structure of the R_2T_{17} materials which have either a hexagonal or a rhombohedral Th_2Ni_{17} structure. These can be obtained from the structure for RT_5 materials by replacing one third of all the R atoms by pairs of T atoms. This results in a larger unit cell in the basal plane in which the unit cell edge is approximately $a\sqrt{3}$, where a is the [100] lattice parameter of the RT_5 hexagonal unit cell. The unit cell in the basal plane in reciprocal space is therefore smaller than that of the other compounds; this is shown in Fig. 4. The layers are then shifted slightly sideways and stacked either in a hexagonal arrangement (Y_2Co_{17}) or in a rhombohedral arrangement (Nd_2Co_{17}) with respectively approximately two or three times the lattice parameter of the RT_5 material. A hexagonal unit cell is used here to describe both the hexagonal and rhombohedral structures with the hexagonal [0001] axis along the growth direction.

The rhombohedral RT_2, RT_3, and R_2T_{17} structures can form two domains, one with the hexagonal $[0001]_H$ axis ($[111]_C$ direction) parallel to the growth direction, and the second with that axis antiparallel to the growth direction. This is most easily understood by considering the above descriptions. The rhombohedral structures are all made up of three layers of some repeat unit—in the case of RT_3 compounds the repeat unit is a set of four planes based on those of the RT_5 structure. The layers, which we shall label A, B and C, are distinguished by a shift relative to the growth plane and two different domains can form either with the growth order *ABCA*…, ($[0001]_H$ direction parallel to the growth direction) or with growth order *ACBA*… ($[0001]_H$ direction antiparallel to the growth direction). If both domains are present in equal amounts the $(1\,0\,\bar{1}\,l_1)$ and $(\bar{1}\,0\,1\,l_2)$ Bragg reflections will be the same, with $l_1 = l_2 = 3n+1, 3n+2$, whereas if only one domain is present then $l_1 = 3n+1$ and $l_2 = 3n+2$, where n is an integer.

The intensities of the Bragg reflections for RT_2, RT_3, and R_2T_{17} were calculated using the atomic positions of the $MgCu_2$ structure given on the Crystal Lattice Structures web page,[15] provided by the Center for Computational Materials Science of the United States Naval Research Laboratory for the RT_2 materials, those of YCo_3 given in Ref. 16 for the RT_3 materials and those of Nd_2Co_{17} and Er_2Co_{17} given in Ref. 17 for the hexagonal and rhombohedral R_2T_{17} structures. The results were corrected for the experimental conditions as follows. A horizontal resolution function was calculated by modeling the Bragg reflections as sharp in q_Z but with a width of $\simeq 1°$ (the mosaic spread) in q_x and considering 2θ to vary by an amount equal to the $\frac{1}{4}°$ slit in front of the detector, a factor of $\frac{1}{\sin(\Omega)}$ was included to take account of the variation in the footprint of the beam on the sample and a factor was also included which took account of the vertical divergence of the monochromator and of the outgoing beam. Details are given in the Appendix.

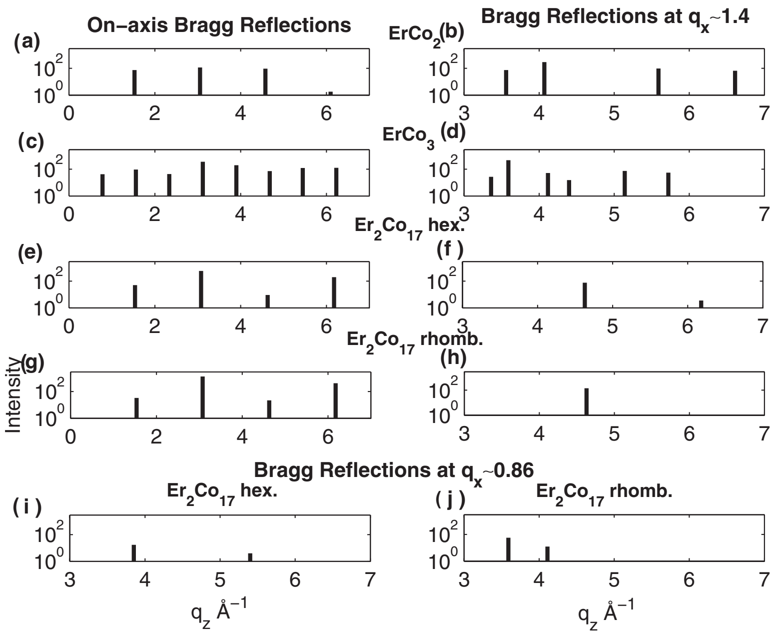

FIG. 5. Approximate intensity predictions from structure factor calculations for longitudinal scans with $q_x=0$, $q_x \simeq 1.4$ and $q_x \simeq 0.86$.

The results of the calculations are shown, for the Er-Co compounds, in Fig. 5. This shows an on-axis scan for each of the materials along the [0001] direction in Figs. 5(a), 5(c), 5(e), and 5(g), the $(1\ 0\ \bar{1}\ l)$ [RT$_2$, Fig. 5(b) and RT$_3$, Fig. 5(d)] and $(1\ 1\ \bar{2}\ l)$ [R$_2$T$_{17}$, Figs. 5(f) and 5(h)] series of Bragg reflections at $q_x \simeq 1.4$ and for the two R$_2$T$_{17}$ structures, hexagonal and rhombohedral, the results of a longitudinal off-axis scan at $q_x \simeq 0.86$ containing the R$_2$T$_{17}$ $(1\ 0\ \bar{1}\ l)$ series of Bragg reflections are shown in Figs. 5(i) and 5(j). The two possible domains produced by stacking the planes in an ABCABC or ACBACB arrangement are averaged.

These diagrams show that observation of the peaks in a longitudinal on-axis scan enables us to distinguish the RT$_3$ structure from that of RT$_2$ and R$_2$T$_{17}$ as the Bragg reflections of RT$_3$ have reflections at $q_z=0.76n$ Å^{-1} while the RT$_2$ and R$_2$T$_{17}$ reflections are at $q_z=1.53n$ Å^{-1} although the reflections with $n=1$ and 3 are very weak in the Er$_2$Co$_{17}$ structure. The reflections at $q_x \simeq 1.4$ Å^{-1} in Fig. 5 further differentiate between the RT$_2$ and R$_2$T$_{17}$ structures as the RT$_2$ $(1\ 0\ \bar{1}\ l)$ series of Bragg reflections are at $q_z=0.51n$ Å^{-1} with systematic absences when n is divisible by 3 and the $(1\ 1\ \bar{2}\ l)$ reflections of the R$_2$T$_{17}$ structures are at $q_z=1.53n$ Å^{-1}, the same positions as the on-axis reflections. Measurement of the R$_2$T$_{17}$ $(1\ 0\ \bar{1}\ l)$ series of reflections at $q_x \simeq 0.86$ Å^{-1} is necessary to distinguish between the hexagonal and rhombohedral forms of the R$_2$T$_{17}$ structure with hexagonal R$_2$T$_{17}$ having reflections at $q_z=0.76n$ Å^{-1} with systematic absences when $n=2$ giving reflections halfway between the previous reflections and rhombohedral R$_2$T$_{17}$ having reflections at $q_z=0.51n$ Å^{-1} with systematic absences when $n=3$ giving reflections one third and two thirds of the way between the previous reflections. Lattice parameters of the different structures are also slightly different and provide more information to distinguish the structures.

It is of interest to calculate the extent to which RT$_2$ samples are not cubic because this determines the direction of the crystal field anisotropy for the R atoms. In terms of the a and c lattice parameters of the rhombohedral system, the percentage deviation from the original cubic structure is given by,

$$\delta = \frac{(c-\sqrt{6}a)\times 2}{(c+\sqrt{6}a)}, \qquad (1)$$

where a and c are the lattice parameters of the hexagonal unit cell.

B. Rare-earth magnetization

The rare-earth ions in the compounds discussed here are all R^{3+} ions with their outer electrons in the 4f orbitals. The magnetic characteristics of the ions, and hence of the compounds, can be understood by considering the behavior of these 4f electrons. The electrons interact with each other via indirect exchange which is mediated by the conduction electrons and this interaction, along with the strong exchange interaction of the transition metals in our samples, leads to magnetically ordered phases.

In addition to this, the 4f orbitals have highly anisotropic charge clouds and the interaction of these with the electric field of the surrounding crystal gives rise to large anisotropies in the magnetization. It is this magnetic anisotropy which fixes the magnetic structure relative to the crystal axes.

Of further interest to us in studying thin layer systems in which there is likely to be large lattice strain, are magnetoelastic effects. In these systems, the magnetoelastic interactions are due primarily to the variation in the crystal field parameters with the lattice strain and can produce effects such as a change in the easy axis of magnetization in the thin films relative to the bulk compounds.

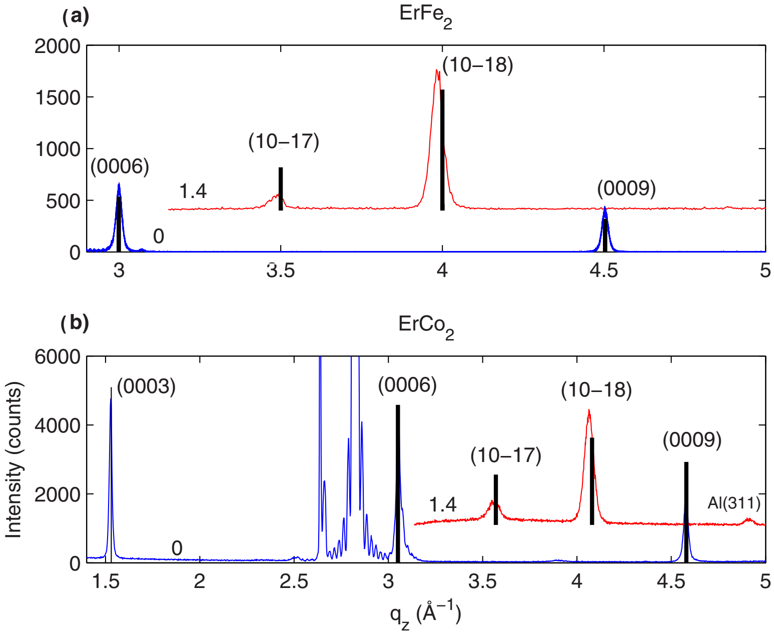

FIG. 6. (Color online) Scattering from longitudinal scans of a) ErFe$_2$ and b) ErCo$_2$. Data marked 0 has $q_x=0$ Å^{-1}, data marked 1.4 has $q_x=1.490$ Å^{-1} (ErFe$_2$) and $q_x=1.433$ Å^{-1} (ErCo$_2$).

IV. RESULTS

The samples were fixed to an aluminum mount with the growth direction horizontal and in the scattering plane and the scattering from the samples was measured by varying the wave-vector transfer both perpendicular to the growth planes of the sample (this direction was defined as q_z) and in the sample growth plane (this direction was defined as q_x). Measurements of the positions of Bragg reflections for the Mo buffer layer and the intermetallic layers showed that the epitaxial relationships are: $[11\bar{2}0]$ sapphire$\parallel[110]$Mo$\parallel[0001]$ RT$_2$ RT$_3$ RT$_5$ R$_2$T$_{17}$ and $[0001]$ sapphire$\parallel[1\bar{1}1]$Mo$\parallel[2\bar{1}\bar{1}0]$ RT$_2$RT$_3$RT$_5\parallel[10\bar{1}0]$ R$_2$T$_{17}$.

A. RT$_2$ compounds

Figure 6 shows part of the results for longitudinal scans of the single films of ErFe$_2$ and ErCo$_2$. The off-axis longitudinal scans were repeated for both the $(1\,0\,\bar{1}\,l)$ and $(\bar{1}\,0\,1\,l)$ series of Bragg reflections with very similar results, showing that both rhombohedral domains are present with very similar intensities. The ϕ angle was also rotated and for off-axis reflections showed a series of similar peaks occurring every 60° in agreement with the expectations if the hexagonal [0001] axis is the growth axis.

The on-axis peaks at $q_x=1.49$ could then be labeled as the $(0\,0\,0\,l)$ reflections with $l=3n$, where n is an integer and for n not divisible by 3, a systematic absence. The off-axis reflections could be labeled as $(1\,0\,\bar{1}\,l)$ with $l=3n$ a systematic absence, in agreement with the predictions of the model shown in Fig. 5 and the calculated intensities in Fig. 6.

The mosaic spread was measured for the on-axis reflections and found to be $0.9\pm0.2°$ for ErFe$_2$ and $1.4\pm0.2°$ for ErCo$_2$. The positions of the Bragg reflections were fitted by a least-squares fitting program to give the lattice parameters listed in Table I. These correspond to deviations from the bulk cubic structure, δ, of 0.39(25)% for ErCo$_2$ and $-2.0(26)\%$ for ErFe$_2$ (see Table III).

B. RT$_2$ superlattices

In addition to the thin films, two superlattices were studied, $[50\text{ErFe}_2/100\text{YFe}_2]_{40}$ and $[75\text{ErFe}_2/75\text{YFe}_2]_{40}$ and the results are shown in Fig. 7. The difference from the results shown in Fig. 6 is that each Bragg reflection is now formed from four or five distinct superlattice peaks showing that the superlattice was of high quality. The separation of the peaks gives the superlattice period as 159 Å and 156 Å, respectively, in good agreement with the nominal periods.

The positions of the peaks were on average close to those of the RT$_2$ samples discussed in the previous section and so it is reasonable to deduce that the structure was rhombohedral with a [0001] direction along the growth axis. This was further supported by a calculation of the intensities of the Bragg reflections which agreed with the measurements. The mosaic spreads of the two superlattices were $1.1\pm0.2°$ and $1.3\pm0.2°$, respectively.

Measurements of the scattering showed that the intensities of the $(1\,0\,\bar{1}\,l)$ reflections were the same as the $(\bar{1}\,0\,1\,l)$ indicating that there was an equal amount of both possible domains. The result of a least-squares fit of the positions of the Bragg reflections gave the lattice parameters of Table I and the anisotropy listed in Table III.

TABLE III. The percentage deviation, δ, of the RT$_2$ compounds from their cubic structure.

Sample	δ (%)
ErFe$_2$	−2.0(26)
ErCo$_2$	0.39(25)
[50ErFe$_2$/100YFe$_2$]	2.1(3)
[75ErFe$_2$/75YFe$_2$]	2.6(3)

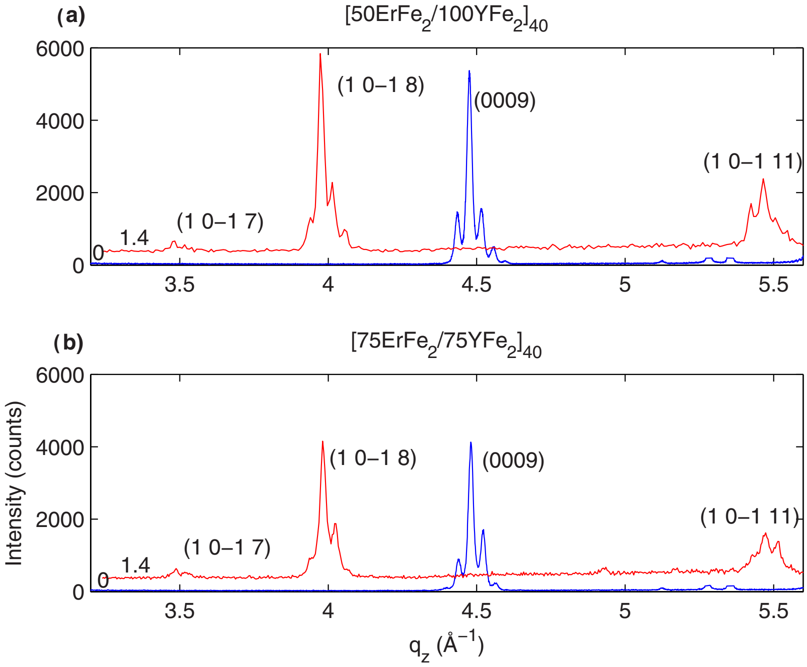

FIG. 7. (Color online) Scattering from a) [50ErFe$_2$/100YFe$_2$] and b) [75ErFe$_2$/75YFe$_2$] longitudinal scans. Data marked 0 has q_x=0 Å, data marked 1.4 has q_x=1.403.

C. RT$_3$ compounds

Figure 8 shows the scattering from ErCo$_3$ and NdCo$_3$ for both on-axis and off-axis scans. The on-axis scans show peaks with a regular repeat of 0.78 Å^{-1} and the off-axis $(1\,0\,\bar{1}\,l)$ scans have peaks at the one third and two third positions between the regular repeats of the on-axis scan. In contrast the $(1\,1\,\bar{2}\,l)$ scattering has peaks at the same values of l as for the on-axis peaks. These results are entirely in agreement with the predictions of the RT$_3$ structure discussed in Sec. III A and in Fig. 8 the peaks have been labeled in terms of the Bragg reflections of the rhombohedral structure of RT$_3$.

For ErCo$_3$, ϕ scans were performed for some of the $(1\,0\,\bar{1}\,l)$ peaks and scattering was observed for ϕ $=0,60,120°,\ldots$ In addition, ϕ scans were also performed on the $(1\,1\,\bar{2}\,l)$ peaks where the maxima occurred at $\phi=-30,30,90°,\ldots$ midway between the peaks of the $(1\,0\,\bar{1}\,l)$ off-axis scan. Although this is as expected for the ErCo$_3$ structure the $(1\,0\,\bar{1}\,l)$ peaks in Fig. 8 are much broader than those for the $(0\,0\,0\,l)$ and $(1\,1\,\bar{2}\,l)$ scans. This suggests that the ordering of the three plane stacking of the layers in ErCo$_3$ is less good than the regular repeat of the unit cell. The mosaic spread of the on-axis peaks was $0.8\pm0.1°$.

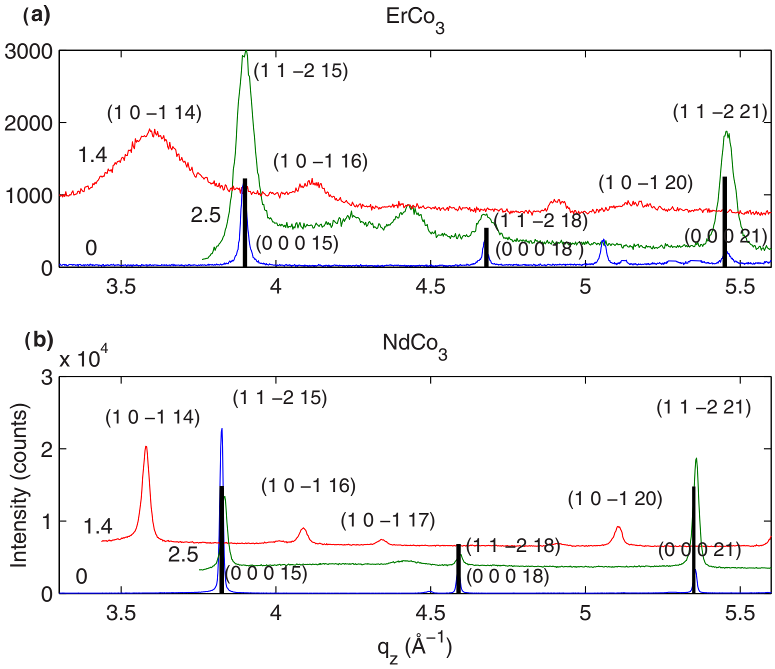

FIG. 8. (Color online) Scattering from a) ErCo$_3$ and b) NdCo$_3$ longitudinal scans. Data marked 0 has q_x=0 Å^{-1}, data marked 1.4 has q_x=1.435 Å^{-1} (ErCo$_3$) and q_x=1.434 Å^{-1} (NdCo$_3$), data marked 2.5 has q_x=2.496 Å^{-1} (ErCo$_3$) and q_x=2.479 Å^{-1} (NdCo$_3$).

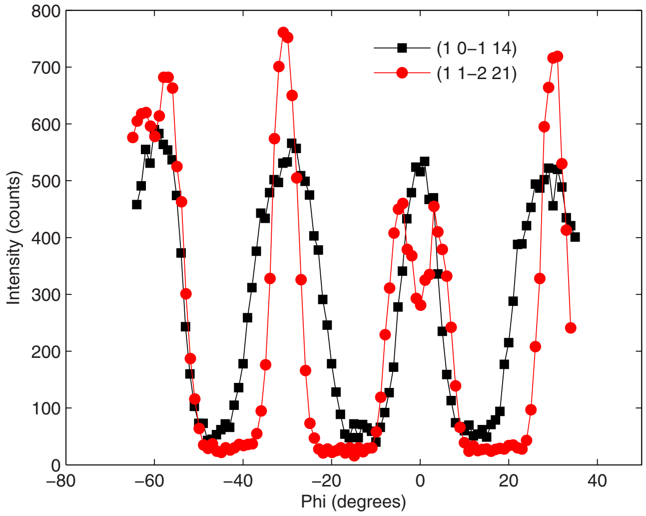

FIG. 9. (Color online) $NdCo_3$ Phi scans at (1,0,14) (squares) and (1,1,21) (circles) reflections.

The x-ray results for $NdCo_3$ were similar to those for $ErCo_3$, as shown in Fig. 8, except that the width of the peaks of the $(1\,0\,\bar{1}\,l)$ scan was only slightly wider than the width of those of the on-axis and $(1\,1\,\bar{2}\,l)$ scans. The ϕ dependence of the intensities was, however, different as shown in Fig. 9. There are well defined peaks for the $(1\,0\,\bar{1}\,l)$ reflections at angles $\phi = -60, 0, 60°, \ldots$ and for the $(1\,1\,\bar{2}\,l)$ reflections at $\phi = -30, 30, 90°, \ldots$ as found in $ErCo_3$. In addition however, there were possibly two peaks separated by 8° for which the center is at −30, 30° for the $(1\,0\,\bar{1}\,l)$ peaks and −60, 0, 60 for the $(1\,1\,\bar{2}\,l)$ peaks. This shows that there are two domains if the structure is rhombohedral or possibly three domains if the structure is tetragonal—although this is less likely. Both of these are surprising if the potential function for the superlattice has minima only at the −60, 0, 60 angles.

SQUID magnetization measurements were made on the $ErCo_3$ and $NdCo_3$ samples, Fig. 10, and, in agreement with the easy axes of the bulk materials, showed that the easy direction of magnetization was along the growth direction [0001] for $ErCo_3$ and perpendicular to the growth direction, i.e., in the growth plane, for $NdCo_3$. There is some noise in the $ErCo_3$ measurements shown in Fig. 10 at $B \simeq \pm 1.5$ T and $B \simeq \pm 3$ T and in the $NdCo_3$ measurements at $B \simeq \pm 4.5$ T. This is due to instrumental problems in measuring extremely small signals since before the diamagnetic contribution of the substrate was subtracted, the measured moment went through zero at these fields.

For the $ErCo_3$ sample it was found that at low temperature, 50 K, and at 5 T, the moment was $1.2 \pm 0.2\mu_B$ per formula unit which is considerably lower than the reported value of $4.2\mu_B$ per formula unit of bulk $ErCo_3$ (Ref. 4) at 4.2 K. However, the measured moment of the epitaxial film can be seen to increase with decreasing temperature implying that better agreement might be found at lower temperatures. The Curie temperature, 195 K, was found to be much lower than the temperature, 395 K reported for bulk $ErCo_3$. This suggests that the thin layer has both the Curie temperature and the moment reduced compared with the bulk values. We have not found any cause for the dramatic decrease in Curie temperature compared to the bulk material.

Measurements on the $NdCo_3$ sample with the applied field parallel to the growth direction showed that the maximum moment at 50 K was $2.5 \pm 0.5\mu_B$ per formula unit which is smaller than the $5.5\mu_B$ per formula unit reported by Buschow[4] for the bulk material. However, when the field

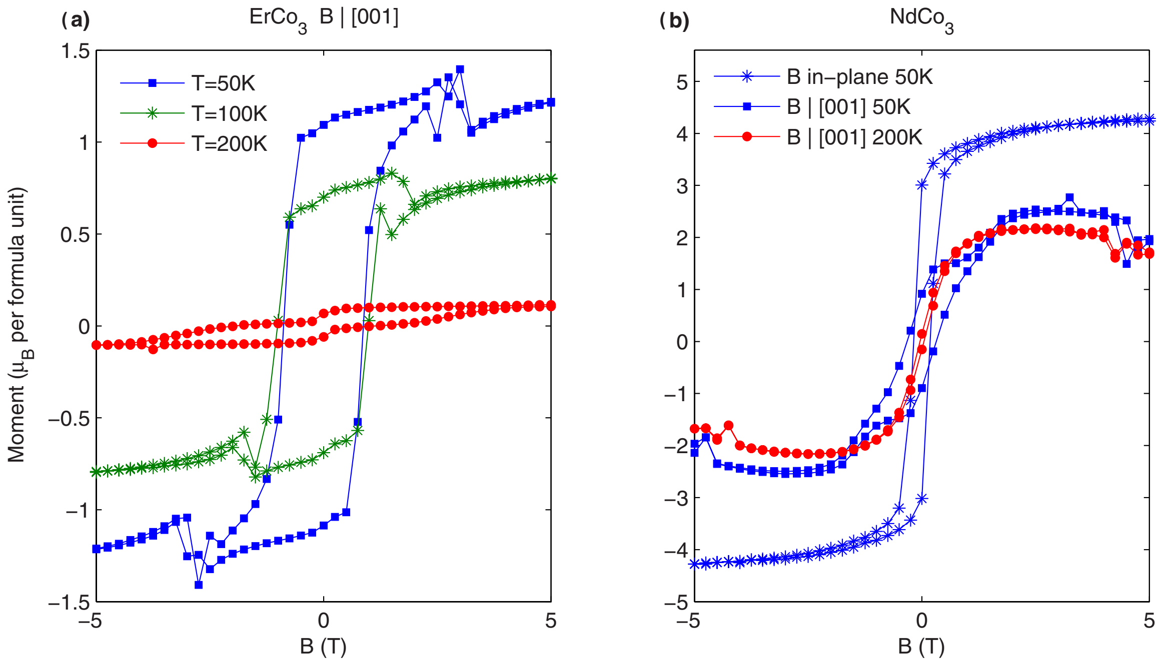

FIG. 10. (Color online) Magnetization measurements for a) $ErCo_3$ and b) $NdCo_3$. The diamagnetic contribution of the sapphire substrate has been subtracted from the data.

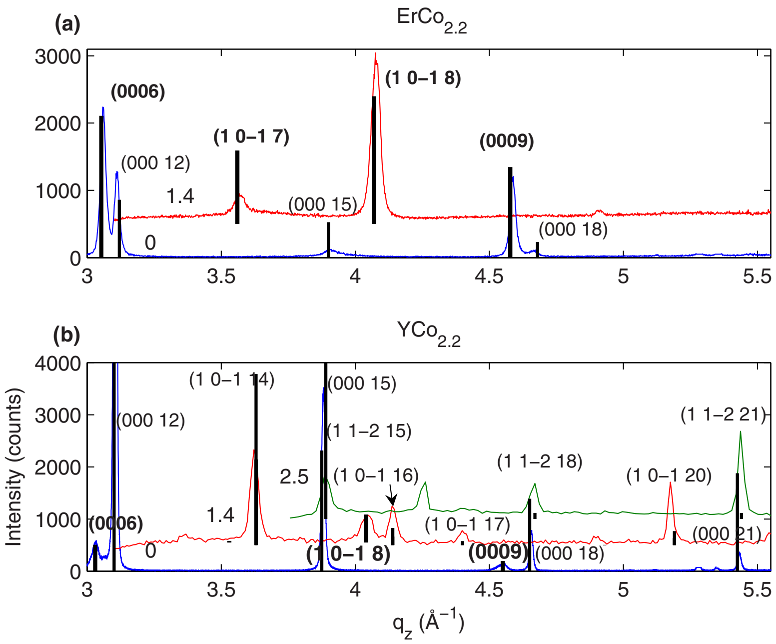

FIG. 11. (Color online) a) $ErCo_{2.2}$ and b) $YCo_{2.2}$ longitudinal scans. Data marked 0 has $q_x=0$ Å^{-1}, data marked 1.4 has $q_x=1.423$ Å^{-1} ($ErCo_{2.2}$) and $q_x=1.425$ Å^{-1} ($YCo_{2.2}$), data marked 2.5 has $q_x=2.477$ Å^{-1} ($YCo_{2.2}$). The labels in bold refer to RT_2 Bragg reflections.

was applied perpendicular to the growth direction, the maximum moment at 50 K was $4.1 \pm 0.4\mu_B$ per formula unit. This is in better agreement with the bulk value but does still suggest that the epitaxial layer has a magnetic moment which is smaller than that of the bulk material. The Curie temperature of the layer is consistent with the temperature found for bulk $NdCo_3$, namely 393 K.

D. Mixed compounds

Growth of $ErCo_{2.2}$ and $YCo_{2.2}$ produced samples containing epitaxial domains of both RT_2 and RT_3 compounds. Figure 11 shows longitudinal scans of the $ErCo_{2.2}$ sample and the on-axis scan has two series of peaks with $q_z=0.77n$ Å^{-1} and $q_z=1.53n$ Å^{-1} where n is an integer. These peaks can be labeled as the peaks arising from the scattering by the RT_2 and RT_3 structures. The results were confirmed for the RT_2 structure by off-axis scans which showed that the structure of the RT_2 part of the sample was rhombohedral.

Similar results were obtained for the $YCo_{2.2}$ sample, which showed peaks in a longitudinal on-axis scan at $1.52n$ Å^{-1} and $0.78n$ Å^{-1} and peaks in an off-axis scan with $q_x=1.425$ Å^{-1} at q_z wave vectors one third and two thirds of the distance between the RT_3 on-axis peaks and a peak from the RT_2 structure. These results and the mosaic spreads of the samples are shown in Table IV. The results show that the growth process produces the two compounds as epitaxial phases rather than as randomly oriented inclusions.

E. RT_5 compounds

X-ray measurements were made of the RT_5 samples, $ErCo_5$, $NdCo_5$ and YCo_5 but they showed only very weak $(0\,0\,0\,l)$ Bragg peaks in longitudinal scans at $q_x=0$ and no $(1\,0\,\bar{1}\,l)$ or $(1\,1\,\bar{2}\,l)$ peaks were found. The positions of the $(0\,0\,0\,l)$ peaks were consistent with the hexagonal structure of the bulk compounds and gave [0001] lattice constants of $c=4.0528(4)$, $c=4.079(5)$, and $c=4.072(9)$ for $ErCo_5$, $NdCo_5$, and YCo_5, respectively. We conclude that there was no alignment of the layers perpendicular to the growth direction. This poor growth is not unexpected; the RT_5 composition is not stable except at elevated temperatures and MBE growth was attempted in the hope of overcoming thermodynamic considerations.

F. R_2T_{17} compounds

The intensity observed when the wave-vector transfer was scanned along the growth axis is shown in Fig. 12 for Er_2Co_{17}, Nd_2Co_{17}, and Y_2Co_{17}. For the first two materials there are regular peaks at positions $q_z=1.53\pm0.01$ Å^{-1} as predicted by the theory described in Sec. III A. The results for the Y_2Co_{17} material are different and the strongest peaks are in the same sequence but at a slightly smaller spacing while there are additional peaks with a spacing of 0.77 ± 0.01 Å^{-1}. These latter peaks are consistent with the YCo_3 phase and we suspect that the growth fluxes used to grow this sample had a flux of Y which was higher than expected and the layer produced was partly Y_2Co_{17} and a smaller quantity of YCo_3. This and our failure to grow good crystals of RT_5 strongly suggest that single phase materials between RT_3 and R_2T_{17} cannot be grown by MBE techniques.

TABLE IV. Structures and mosaic spreads of compounds found in the $YCo_{2.2}$ and $ErCo_{2.2}$ samples.

Compound	Structure	a (Å)	c (Å)	Mosaic (°)
$ErCo_2$	$MgCu_2$ (*r.*)	5.100(18)	12.322(24)	1.4(2)
$ErCo_3$	$PuNi_3$ (*r.*)		24.229(24)	0.85(15)
YCo_2	$MgCu_2$ (*r.*)		12.439(12)	0.8(1)
YCo_3	$PuNi_3$ (*r.*)	5.004(17)	24.2969(13)	0.4(1)

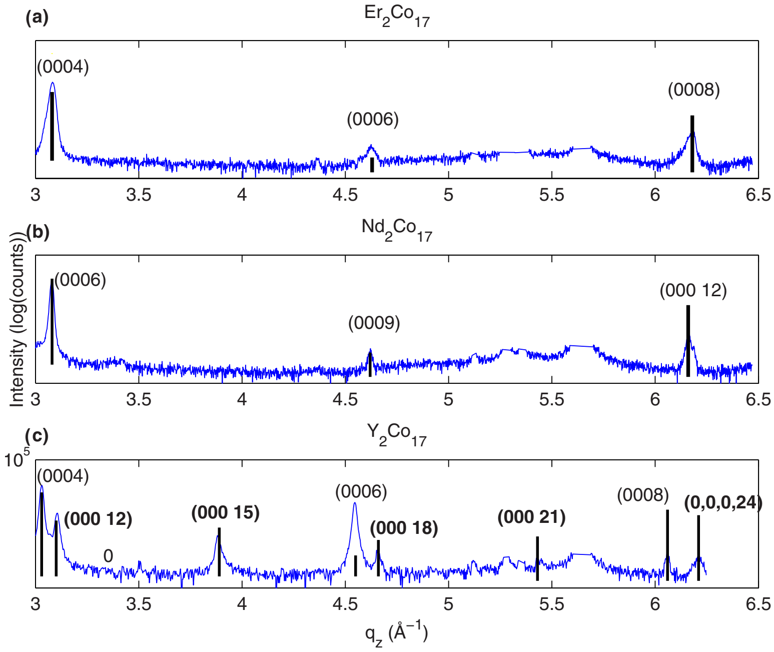

FIG. 12. (Color online) a) Er_2Co_{17}, b) Nd_2Co_{17} and c) Y_2Co_{17} on-axis longitudinal scans. The labels in bold refer to YCo_3 Bragg reflections.

Off-axis scans of the $(1\,1\,\bar{2}\,l)$ and $(3\,0\,\bar{3}\,l)$ series of Bragg reflections are shown in Fig. 13 for Er_2Co_{17} and Nd_2Co_{17}. For these off-axis scans q_x=1.49 Å and q_x =2.61 Å, respectively, because the in-plane lattice parameter is larger for the R_2T_{17} compounds than for the other structures. The scans show Bragg scattering at the same positions as the on-axis scans as predicted by the theory in Sec. III A. In order to determine whether the structures are rhombohedral or hexagonal, the off-axis reflections $(1\,0\,\bar{1}\,l)$ or $(2\,0\,\bar{2}\,l)$ need to be measured. Our measurements of these off-axis scans had no peaks at either the positions predicted for the rhombohedral or those for the hexagonal structures. We conclude that there is no long-range order in the orientation of the layers in this structure and that the only Bragg peaks that can be observed are those which are independent of the stacking sequence. Nevertheless we have labeled the peaks in Figs. 12 and 13 using the structures of the bulk material in which Er_2Co_{17} and Y_2Co_{17} are hexagonal and Nd_2Co_{17} is rhombohedral.

Magnetization measurements were made for Er_2Co_{17} and Nd_2Co_{17}. Some of the measurements are shown in Fig. 14 with the susceptibility of the diamagnetic sapphire substrate removed. However, while we expect the samples to be saturated at high fields, instead the Er_2Co_{17} sample has a decreasing moment and the Nd_2Co_{17} sample has an increasing mo-

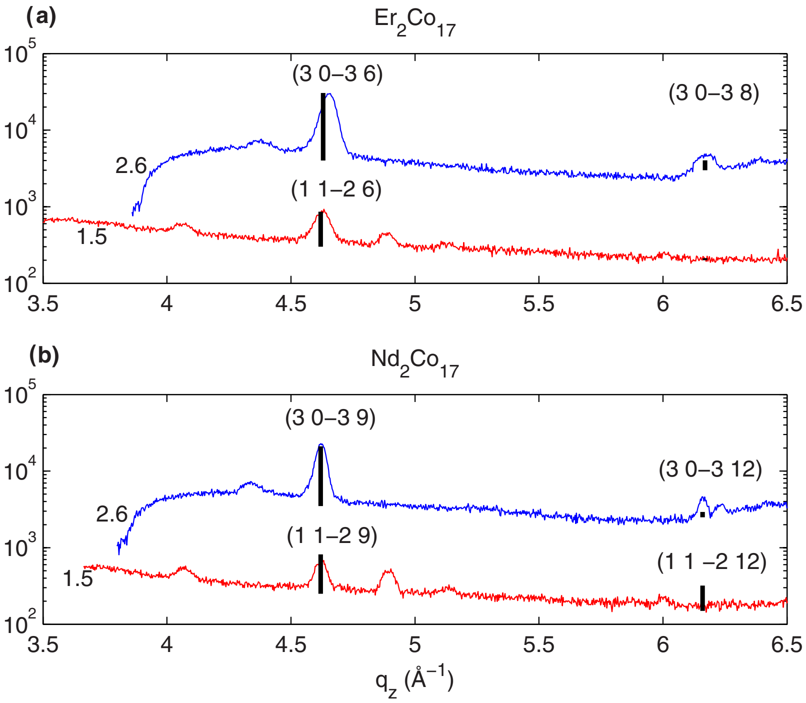

FIG. 13. (Color online) a) Er_2Co_{17} b) and Nd_2Co_{17} off-axis longitudinal scans. Data marked 1.5 has q_x=1.510(4) $Å^{-1}$ (Er_2Co_{17}) and q_x =1.489(3) $Å^{-1}$ (Nd_2Co_{17}), data marked 2.6 has q_x=2.610(5) $Å^{-1}$ (Er_2Co_{17}) and q_x =2.583(4) $Å^{-1}$ (Nd_2Co_{17}).

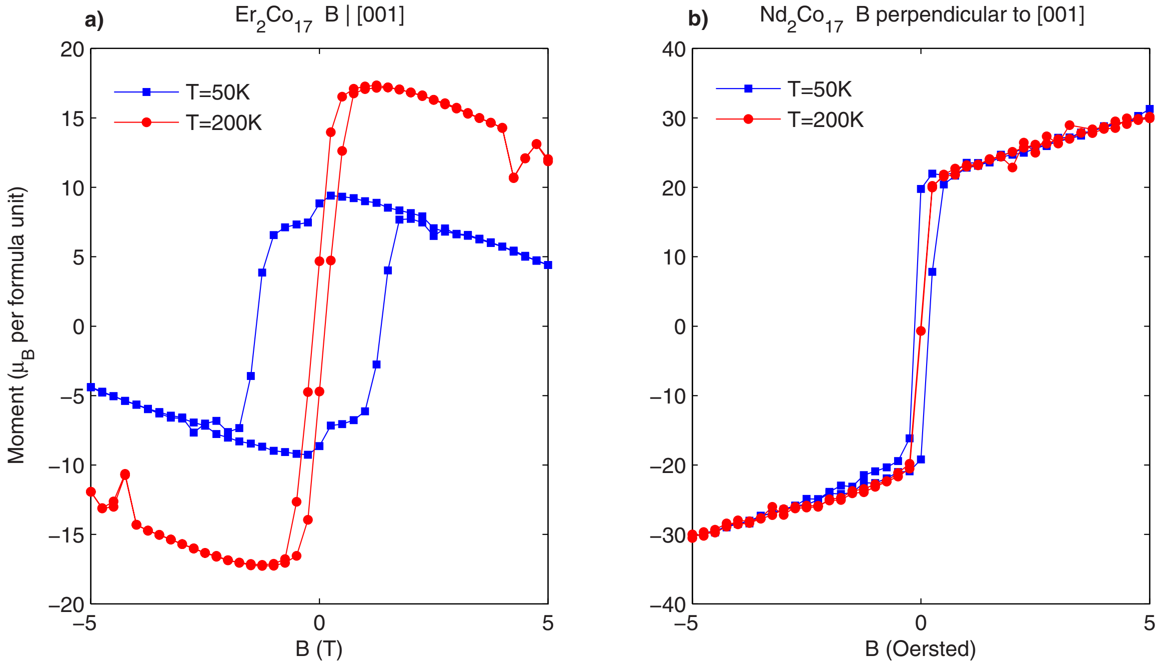

FIG. 14. (Color online) Magnetization measurements for Nd_2Co_{17} and Er_2Co_{17} at $T=50$ and 200 K. The diamagnetic contribution of the sapphire substrate has been subtracted from the data.

ment. This would occur if the susceptibility of the sapphire substrate in these samples (which is very large in comparison to the magnetization of the R_2T_{17} film) was slightly different from the previously measured value (see Sec. II C).

It was found that the easy axis of the magnetization was parallel to the growth direction for Er_2Co_{17} and perpendicular to the growth direction for Nd_2Co_{17}. These orientations are in agreement with those of the bulk media. In a field of 5 T the moment for Er_2Co_{17} was $10\pm1.5\mu_B$ at 50 K and $19\pm2\mu_B$ at 200 K. The 50 K value agrees well with the low-temperature bulk value of $20\mu_B$ given in Ref. 4 and as our measured moment increases with increasing temperature, the higher value at 220 K is not unreasonable. Figure 14 also shows that the Er_2Co_{17} material has a smaller coercive field at higher temperatures, indicating that the Er moment (which has large anisotropy) decreases with increasing temperature. As the Er and Co magnetic moments couple antiferromagnetically, this decrease also accounts for the increase with temperature of the total moment. The moment at 5 T and 50 K for Nd_2Co_{17} was $20\pm3\mu_B$ per formula unit, showing that the epitaxial layer has a magnetic moment which decreased in comparison to the bulk value of $67\mu_B$ per formula unit.

V. CONCLUSION

X-ray diffraction measurements have been made which show that it is possible to grow RT_2 materials by MBE techniques, using a Mo (110) buffer, with the cubic [111] axis as the growth axis. $ErFe_2$ and $ErCo_2$ layers have been produced and in addition superlattices of YFe_2 and $ErFe_2$ have been successfully grown. The structure of these materials is rhombohedral and they are slightly distorted from the bulk cubic structure by having the $[111]_C$ axis slightly elongated or compressed compared with the in-plane lattice constant. We plan to investigate the effect of these distortions on the magnetic structure and anisotropy in the future. The mosaic spread of the above materials is about 1°. A large advantage of this process is that it opens the way to growing materials such as RT_3, RT_5, and R_2T_{17} and we have begun investigating their properties. $ErCo_3$ and $NdCo_3$ layers have been grown even though both materials have a very large unit cell of 24 Å along the *c*-axis. It is surprising that we obtain coherence of this structure over many periods, as detailed in Sec. III A. The structures are rhombohedral and in the case of $ErCo_3$ the reflections that depend on the rhombohedral order have markedly smaller intensities than the reflections that are not sensitive to the layer positions. In the case of $NdCo_3$ the order is well defined in two separate domains in the scattering observed approximately every 30° on rotating about the growth axis instead of the expected 60°. We do not understand why two structures relatively oriented by about 30° should be stable.

Magnetization measurements on $ErCo_3$ suggest that the magnetization is reduced in the layer compared with bulk properties and similar measurements on $NdCo_3$ show the same trend. In addition to this, the easy axes are the same as for the bulk media, suggesting that the magnetic anisotropy of the samples is unchanged from that of bulk compounds. However, measurements of the Curie temperature of $ErCo_3$ showed a decrease from the bulk temperature of 395 K to 195 K while the Curie temperature of the $NdCo_3$ sample was found to be consistent with the bulk temperature of 393 K. Although it is not clear why such a decrease should be seen only in the Er compound, there are differences in the magnetic properties of $ErCo_3$ and $NdCo_3$ such as the easy direction of magnetization and the parallel/antiparallel coupling of the R and T moments that would allow different interactions in the two compounds. However, we have found nothing to explain such a marked decrease in the Curie temperature.

R_2T_{17} compounds such as Er_2Co_{17} and Nd_2Co_{17} were grown and have a highly ordered hexagonal structure. Within this structure it was not possible to determine the stacking sequence of the atomic planes and we suspect that there is a random sequence of the three possible stacking positions with the requirement that the same plane cannot repeat itself immediately. Magnetization measurements on Er_2Co_{17} show that the magnetization of the layer is similar to that of the bulk material while the magnetization of the Nd_2Co_{17} layer is smaller than that of the bulk. For both compounds, the easy direction of the magnetization is the same for the single layer as for the bulk compounds.

Our results show that we could not grow RT_5 materials. These materials have the simplest crystal structure but are not thermodynamically stable at the growth temperatures used. It was found that it was not possible to overcome the thermodynamics of the system using the MBE growth process described.

Somewhat surprising is the result of growing $RT_{2.2}$ materials and Y_2Co_{17} materials with an excess of Y. In both cases we found that the material separated into two commensurate epitaxial phases: RT_2+RT_3 and R_2T_{17}+RT_3. It is interesting that the two compounds should grow epitaxially rather than as randomly oriented inclusions.

Finally we plan further developments to study the new materials we have grown including further work on the magnetic properties and to investigate whether we can grow RT_2-RT_3 as coherent superlattices. We hope that this paper will stimulate future work.

APPENDIX

In this paper we have described the use of the MRD to measure the x-ray scattering. We must therefore calculate the proportionality constants that connect the structure factors to the observed intensity. The MRD was mostly used with a highly collimated incident beam, ~0.002°, and a slit defining the scattered beam, ~0.25°, and the mosaic spreads were typically 1°. Consequently in the analysis we need to consider in the horizontal plane only the effects of the outgoing slit and the mosaic spread. We shall then include the effect of the mosaic spread perpendicular to the scattering plane and the beam footprint on the sample.

Figure 15 shows a scattering diagram for the MRD with the same axes as used in the body of the paper. The diffractometer is aligned around a Bragg reflection which is at (τ_x, τ_z). The angle α is the small angle allowed through the detector slit and gives rise to the resolution line in reciprocal space. If the distance along the line is given by

$$q = k\alpha, \tag{A1}$$

it has components

$$q_x = -k\alpha \sin(\phi + \theta - 90), \tag{A2}$$

$$q_z = k\alpha \cos(\phi + \theta - 90), \tag{A3}$$

showing that the line of the resolution function in reciprocal space is given by

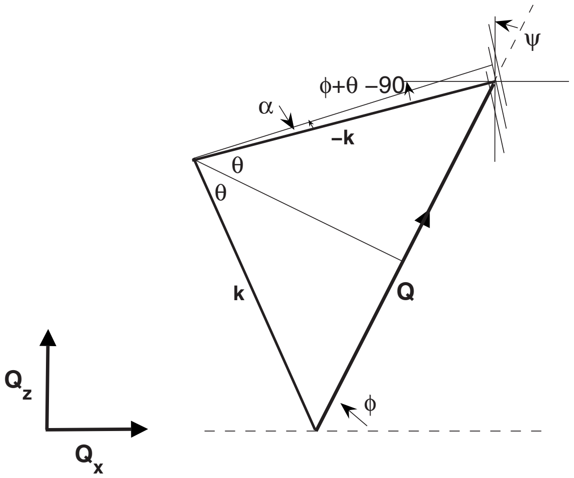

FIG. 15. Reciprocal space diagram for the intensity of Bragg reflections defining 2θ, ψ, ϕ, Q_x and Q_z.

$$q_z \sin(\phi + \theta - 90) + q_x \cos(\phi + \theta - 90) = 0, \tag{A4}$$

while the intensity depends on the position on the line and will be approximated by a normalized Gaussian,

$$M_1(q) = \frac{1}{\sqrt{\pi} k\Delta} \exp\left(-\frac{q^2}{(\Delta k)^2}\right), \tag{A5}$$

where the width Δ denotes the width of the slit.

The width of the scattering is experimentally found to be mostly perpendicular to the z axis corresponding to an anisotropic mosaic spread characteristic of these layer systems. We shall assume the width is proportional to the z component of the Bragg reflection, its width in wave vector is therefore $p = \beta\tau_z$ and in terms of the x and z components is $p_x = \beta\tau_z$ and $p_z = 0$. The probability of the angle β is given by a normalized Gaussian and we obtain for a width Δ_s

$$M_s(p) = \frac{1}{\sqrt{\pi}\Delta_s \tau_z} \exp\left(-\frac{p^2}{(\Delta_s \tau_z)^2}\right). \tag{A6}$$

The intensity at the maximum of the different Bragg reflections is given by the product of Eqs. (A5) and (A6) with $q = p = 0$ to give

$$I_{\max} = \frac{1}{\pi \Delta \Delta_s \tau_z k}. \tag{A7}$$

The intensity of the Bragg reflections is frequently measured by integrating the intensity as the wave-vector transfer is varied through the Bragg reflection. We assume that the scan makes an angle ψ with respect to the z axis and denote the trajectory by a wave vector Q and the angle ψ. The components of the wave vector are $(Q \sin \psi, Q \cos \psi)$.

The scattering intensity occurs where the experimental resolution intersects the scattering which implies that the q_z of the resolution must be equal to the Q_z of the scan of the wave vector. This in turn implies that $q_z = Q \cos \psi$ so that, from Eq. (A4),

$$q_x = -Q \cos \psi \tan(\phi + \theta - 90), \tag{A8}$$

and the total length of resolution q is then

$$q = Q\cos\psi[\tan^2(\phi+\theta-90)+1]^{1/2}. \tag{A9}$$

Now these expressions can be substituted into the probability functions to give

$$M(Q) = \frac{1}{\pi\Delta\Delta_s\tau_z k}\exp\left\{-Q^2\cos^2\psi \times \left[\frac{(\tan^2(\phi+\theta+90)+1)}{(\Delta^2 k^2)} + \frac{\tan^2(\phi+\theta+90)}{(\Delta_s^2\tau_z^2)}\right]\right\}. \tag{A10}$$

This expression has a Gaussian width given by

$$W(Q) = \left[\tan^2(\phi+\theta-90)\cos^2\psi \times \left(\frac{1}{k^2\Delta^2}+\frac{1}{\Delta_s^2\tau_z^2}\right) + \frac{\cos^2\psi}{k^2\Delta^2}\right]^{-(1/2)} \tag{A11}$$

and an integrated intensity of

$$I = \frac{W(Q)}{\sqrt{\pi}\Delta\Delta_s k\tau_z}. \tag{A12}$$

The vertical divergence was calculated including the spread in scattering of the Bragg peaks by Axe and Hastings.[18] The result is given by

$$I_v = \left[1 + \frac{4\Delta_s^2\sin(90+\theta-\phi)\sin(\theta+\phi-90)}{\Delta_\mu^2+\Delta_A^2}\right]^{-(1/2)}, \tag{A13}$$

where Δ_s is the width of the sample scattering, Δ_μ is the monochromator vertical divergence and Δ_A is that of the analyzer.

The beam footprint for a layer system is a factor proportional to

$$I_F = \sin(90+\theta-\phi)^{-1} \tag{A14}$$

because for a layer system larger than the beam, the illuminated area is the appropriate surface volume.

The result for the peak intensity is the product of the expressions (A7), (A13), and (A14) while for the integrated intensity it is (A12)–(A14).

---

*r.jones1@physics.ox.ac.uk

[1] J. M. D. Coey, Solid State Commun. **102**, 101 (1997).
[2] R. Skomski and J. M. D. Coey, Phys. Rev. B **48**, 15812 (1993).
[3] T. Ando and T. Nishihara, IEEE Trans. Magn. **33**, 2983 (1997).
[4] K. H. J. Buschow, Rep. Prog. Phys. **40**, 1179 (1977).
[5] R. Ward, M. Wells, C. Bryn-Jacobsen, R. Cowley, J. Goff, D. McMorrow, and J. Simpson, Thin Solid Films **275**, 137 (1996).
[6] D. F. McMorrow, P. P. Swaddling, R. A. Cowley, R. C. C. Ward, and M. R. Wells, J. Phys.: Condens. Matter **8**, 6553 (1996).
[7] M. Sawicki, G. J. Bowden, P. A. J. de Groot, B. D. Rainford, J.-M. L. Beaujour, R. C. C. Ward, and M. R. Wells, Phys. Rev. B **62**, 5817 (2000).
[8] M. J. Bentall, R. A. Cowley, W. J. L. Buyers, Z. Tun, W. Lohstroh, R. C. C. Ward, and M. R. Wells, J. Phys.: Condens. Matter **15**, 4301 (2003).
[9] K. N. Martin, K. Wang, G. J. Bowden, A. A. Zhukov, P. A. J. de Groot, J. P. Zimmermann, H. Fangohr, and R. C. C. Ward, Appl. Phys. Lett. **89**, 132511 (2006).
[10] F. Robaut, P. Milkulik, N. Cherief, O. F. K. McGrath, D. Givord, T. Baumbach, and J. Y. Veuillen, J. Appl. Phys. **78**, 997 (1995).
[11] E. E. Fullerton, J. S. Jiang, C. Rehm, C. H. Sowers, S. D. Bader, J. B. Patel, and X. Z. Wu, Appl. Phys. Lett. **71**, 1579 (1997).
[12] J. J. Keavney, E. E. Fullerton, J. E. Pearson, and S. D. Bader, J. Appl. Phys. **81**, 4441 (1997).
[13] F. Robaut, S. Jaren, N. Cherief-Benbrahim, and C. Meyer, Appl. Phys. Lett. **69**, 1643 (1996).
[14] M. Huth and C. P. Flynn, Phys. Rev. B **58**, 11526 (1998).
[15] http://cst-www.nrl.navy.mil/lattice/struk/laves.html
[16] J. F. Smith and D. A. Hansen, Acta Crystallogr. **19**, 1019 (1965).
[17] W. Ostertag and K. J. Strnat, Acta Crystallogr. **21**, 560 (1966).
[18] J. D. Axe and J. B. Hastings, Acta Crystallogr. **39**, 593 (1983).